
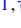


Angle-resolved photoemission spectroscopy study of charge density wave order in the layered semiconductor EuTe₄

Chen Zhang,¹ Qi-Yi Wu,¹ Ya-Hua Yuan,¹ Xin Zhang,^{2,3} Hao Liu,¹ Zi-Teng Liu,¹ Hong-Yi Zhang¹,, Jiao-Jiao Song,¹ Yin-Zou Zhao,¹ Fan-Ying Wu,¹ Shu-Yu Liu,¹ Bo Chen,¹ Xue-Qing Ye,¹ Sheng-Tao Cui,⁴ Zhe Sun,⁴ Xiao-Fang Tang,⁵ Jun He,¹ Hai-Yun Liu,⁶ Yu-Xia Duan,¹ Yan-Feng Guo,^{2,3,*} and Jian-Qiao Meng^{1,†}

¹*School of Physics and Electronics, Central South University, Changsha 410083, Hunan, China*

²*School of Physical Science and Technology, ShanghaiTech University, Shanghai 201210, China*

³*ShanghaiTech Laboratory for Topological Physics, ShanghaiTech University, Shanghai 201210, China*

⁴*National Synchrotron Radiation Laboratory, University of Science and Technology of China, Hefei 230029, Anhui, China*

⁵*Department of Physics and Electronic Science, Hunan University of Science and Technology, Xiangtan 411201, Hunan, China*

⁶*Beijing Academy of Quantum Information Sciences, Beijing 100085, China*



(Received 16 March 2022; revised 28 October 2022; accepted 7 November 2022; published 16 November 2022)

Layered tellurides have been extensively studied as a platform for investigating the Fermi surface (FS) nesting-driven charge density wave (CDW) states. EuTe₄, one of the quasi-two-dimensional binary rare-earth tetratelluride CDW compounds with unconventional hysteretic transition, is currently receiving much attention. Here, the CDW modulation vector, momentum, and temperature dependence of CDW gaps in EuTe₄ are investigated using angle-resolved photoemission spectroscopy. Our results reveal that (i) a FS nesting vector $\mathbf{q} \approx 0.67\mathbf{b}^*$ drives the formation of the CDW state, (ii) a large anisotropic CDW gap is fully open in the whole FS and maintains a considerable size even at 300 K, leading to the appearance of semiconductor properties, (iii) an abnormal behavior of CDW gap in magnitude as a function of temperature, and (iv) an extra, larger gap opens at higher binding energy due to the interaction between the different orbits of the main bands.

DOI: [10.1103/PhysRevB.106.L201108](https://doi.org/10.1103/PhysRevB.106.L201108)

The interactions among charge, spin, orbit, and lattice in solids lead to abundant exotic quantum phenomena [1], such as charge density wave (CDW) [2–4], high-temperature superconductivity [5], heavy fermions [6], and so on. These orders are often entangled with each other. For example, in the past two decades, CDW order has been proven to have a complex interplay, competition, or coexistence, with superconducting order at low temperatures, especially in unconventional superconductors [7–11]. Understanding the formation mechanism of CDW is of great importance to understanding their interaction with other orders and is also the key to understanding and controlling the collective motion of CDW orders.

In a one-dimensional system, the Fermi surface (FS) nesting mechanism proposed by Peierls has successfully explained the formation of CDW. Briefly, the FS nesting mechanism means that one section of FS can completely coincide with another FS after translating by a wave vector \mathbf{q}_{CDW} , resulting in the redistribution of electron density in the new periodic field and the opening of a complete gap at Fermi energy (E_F) [3,4,12]. However, almost no perfect FS nesting occurs in two-dimensional (2D) and three-dimensional (3D) systems. The imperfect FS nesting causes partial energy gap opening and FS reconstruction, leaving residual electronic pockets so that the system maintains a metallic state in the CDW phase [13–16].

Telluride is the representative of chalcogenide compounds with a large number of family members, including monotellurides [17], ditelluride [18–21], tritellurides [14–16,22–25], tetratellurides [26], etc. CDW states driven by FS nesting have been widely found in many quasi-2D polytellurides [14–16,21–24,26], making it an ideal platform for studying CDW sequences.

Recently, a novel quasi-2D binary rare-earth tetratelluride with CDW phase, EuTe₄, was reported [27]. The CDW phase in EuTe₄ has been confirmed by transmission electron microscopy (TEM) and x-ray diffraction, which identified an incommensurate modulation wave vector $\mathbf{q} = 0.643(3)\mathbf{b}^*$ (where $\mathbf{b}^* = \frac{2\pi}{b}$) [28]. Figure 1(a) shows the crystal structure of EuTe₄. In contrast to RTe₃ ($R = \text{Dy-Lu}$) [14–16], an additional Te-Te square-net plane is inserted into the adjacent Eu-Te slabs, which causes EuTe₄ to contain two types of Te planes: bilayer and monolayer separated by the EuTe layer. It was considered that the CDW modulation of rare-earth tellurides comes from Te square layers [15,16]. Thus, there would be a relative difference in CDW distortion between these two different types of Te square layers, which causes some novel characteristics associated with CDW that are significantly distinct from the RTe₃ compounds [28,29]. A significant temperature hysteresis loop was observed in EuTe₄ [27,28], which closely relates to 3D configurations of the in-plane density waves [28]. The temperature-dependent resistivity measurements on EuTe₄ show typical semiconductor behavior rather than metallic behavior in the CDW state [27,28]. Theoretical calculation of electronic susceptibility

*Corresponding author: guoyf@shanghaitech.edu.cn

†Corresponding author: jqmeng@csu.edu.cn

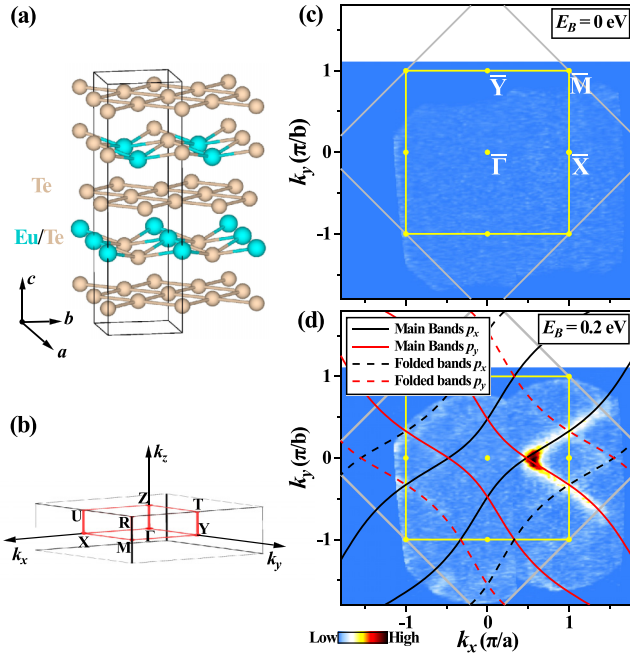


FIG. 1. (a) The crystal structure of EuTe_4 . (b) A 3D reduced Brillouin zone (BZ) of EuTe_4 with high symmetry points marked. (c) and (d) Constant energy contours at the E_F and at 0.2 eV below E_F as a function of k_x and k_y measured at a temperature of 30 K. The solid yellow squares outline the projected first BZ of the 3D crystal structure, and the solid gray squares represent the extended BZ formed by the Te square net. The black (p_x) and red (p_y) solid lines in (d) are the expected bands from the Te square net calculated by the TB model, and the corresponding dashed lines represent the folded bands.

suggests that the monolayer and bilayer Te layers primarily contribute to FS nesting and electronic instability, respectively, to drive the formation of CDW in EuTe_4 [29].

In this Letter, we present a detailed angle-resolved photoemission spectroscopy (ARPES) study of the electronic structure and CDW gap in EuTe_4 as a function of temperature and momentum. It is found that a large anisotropic CDW gap is fully open in the whole FS and therefore had no spectral weight around E_F , thus resulting in its semiconducting properties. The low-lying electronic structure is the linearly dispersive bands dominated by the Te 5p band derived from Te square nets. We consider that the imperfect FS nesting drives the formation of the CDW state in EuTe_4 . The data reveals that the CDW gap has strong momentum and temperature dependence. Moreover, the CDW gap persists even at room temperature, and its temperature dependence deviates from the prediction of traditional CDW theory.

High-quality EuTe_4 single crystals were grown via the Te self-flux approach [30]. ARPES measurements were performed at the ARPES beamline (BL13U) of the National Synchrotron Radiation Laboratory, Hefei, with a Scienta Omicron DA30L analyzer. All samples used in this study were cleaved *in situ* and measured in an ultrahigh vacuum with a base pressure better than 6×10^{-11} Torr. The energy and angular resolutions were better than 20 meV and 0.3° , respectively. The Fermi level is referenced by measuring clean

polycrystalline Au that is electrically connected to the sample. All data were taken with 35 eV photons.

As presented in Fig. 1(c), the measured FS of EuTe_4 at 30 K shows no intensity contrast, indicating that the whole FS is fully gapped. It is consistent with its semiconductor characteristics in transport measurement. Figure 1(d) displays the constant energy contour at binding energy $E_B = 0.2$ eV, and an apparent twofold symmetry of the low-lying electronic structure can be seen. Calculation suggested that the Eu 4f electrons are localized around 1.5 eV below E_F [27], and the electronic states near the E_F are dominated by the 5p orbitals of Te atoms on the Te-Te plane [27–29,31,32]. Thus, similar to the RTe_3 , the low-lying band structure of EuTe_4 can be described by an elementary 2D tight-binding (TB) model, which only includes the in-plane p_x and p_y orbitals of the Te plane and contains no hybridization between them [15,16,33]. Using the axes of the 3D BZ, this model yields dispersions for p_x and p_y as the following equations [16,23]:

$$E_{p_x}(\mathbf{k}) = -2t_{\parallel} \cos\left[(k_x + k_y)\frac{a}{2}\right] + 2t_{\perp} \cos\left[(k_x - k_y)\frac{a}{2}\right] - E_F,$$

$$E_{p_y}(\mathbf{k}) = -2t_{\parallel} \cos\left[(k_x - k_y)\frac{a}{2}\right] + 2t_{\perp} \cos\left[(k_x + k_y)\frac{a}{2}\right] - E_F,$$

where the t_{\parallel} and t_{\perp} are the hopping amplitude along and perpendicular to the p_x orbital, respectively. Otherwise, consider that this TB model is constructed on a single Te plane which is rotated 45° with respect to the unit cell and has only half the area. Therefore, the area of the 2D BZ [gray squares in Fig. 1(d)] for the TB model is twice that of the 3D BZ [yellow squares in Fig. 1(d)], and its periodicity should be folded back with respect to the 3D BZ boundaries to acquire the 3D lattice symmetry. It gives rise to the folded bands along the reduced BZ boundaries shown by the dashed lines in Fig. 1(d). Figure 1(d) compares the measured and simulated FS cross sections at $E_B = 0.2$ eV. It can be seen that the measured and simulated FS cross sections agree with each other very well. On the 3D BZ boundary, an \bar{X} -centered diamondlike pocket formed by crossing the main bands and its folded bands is observed, similar to EuSbTe_3 [34].

Next, we study how the FS contours change for energies below the E_F ; the resulting maps are given in Figs. 2(a1)–2(a4). At each E_B , the TB model and experimental data are excellently consistent, suggesting this model is reasonable for understanding the band structure of EuTe_4 . As E_B increases, the \bar{X} -centered diamondlike pocket keeps shrinking. On the contrary, the spectral intensity around the $\bar{\Gamma}$ point gradually increases, and a larger inner diamond-shaped pocket is gradually formed. The band structure at high E_B is reminiscent of the FS of RTe_3 [16].

Besides the main and folded bands, there are some weak features that we refer to as shadow bands, as indicated by the arrows in Fig. 2(a1). Figure 2(b) shows a series of momentum distribution curves (MDCs) at $E_B = 0.4$ eV along seven evenly spaced cuts (cuts 1–7) as labeled in Fig. 2(a2). It can be seen that the distance between the shadow band peak and the main band peak has a slight variation. That is, the shadow band is nearly parallel to the upper branch of the main band. The shadow band can be roughly produced by shifting the main band by a CDW wave vector $\mathbf{q}_{\text{CDW}} \approx \frac{2}{3}\mathbf{b}^*$, which is consistent with the TEM results [28].

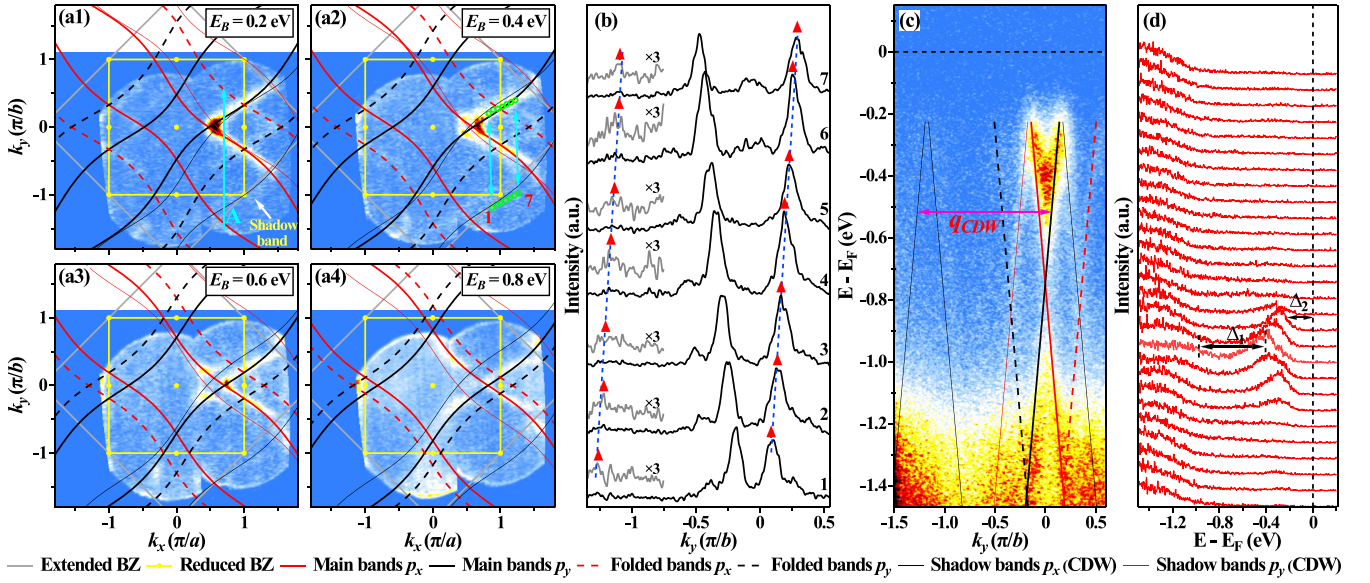


FIG. 2. (a1)–(a4) The constant energy maps integrated over 20 meV, centered at binding energies $E_B = 0.2, 0.4, 0.6$, and 0.8 eV, respectively. (b) MDCs spectra at $E_B = 0.4$ eV for evenly spaced cuts (1–7) as shown in (a2). Note that the signal of the shadow bands is very weak. To see the weak features more clearly, the original MDCs (black lines) are expanded three times (gray lines). The curves are shifted vertically for easy view. The blue dashed lines serve as a guide for the eyes. (c) ARPES image plot of cut A indicated by the cyan arrow shown in (a1). The straight solid and dashed lines represent band dispersion serving as guides for the eyes (see legend). (d) EDCs corresponding to (c), from where two gaps can be observed.

To understand the implications of the transverse CDW on the band structure, a measurement [cyan arrow in Fig. 2(a1)] parallel to the k_y direction at $k_x = 0.35a^*$ ($a^* = \frac{2\pi}{a}$) is taken. The obtained image and the corresponding energy distribution curves (EDCs) are presented in Figs. 2(c) and 2(d), respectively. Combined with the TB model, we can clearly distinguish the dispersion of the main bands (thick solid lines), the folded bands (dashed lines), and the shadow bands (thin solid lines). Two gaps, Δ_1 and Δ_2 , can be observed, as indicated by black double-headed arrows in Fig. 2(d). Δ_1 is opened near the higher binding energy of 0.7 eV. Similar gaps have been observed in some layered rare-earth tellurides, which occur at the crossing point between the main and folded bands [15,16,34]. However, in EuTe_4 , this gap is not a result of the intersection between the main and folded bands but the intersection between the different orbits of the main bands. Δ_2 is located around E_F , which is generally called the CDW gap. As previously reported in many FS nesting-driven CDW materials, the interaction between the main bands and the shadow bands leads to the opening of the CDW gap Δ_2 and leaves a lower branch below E_F . This phenomenon further provides evidence of the validity of FS nesting in determining the CDW instabilities and the semiconducting property in this system.

To quantitatively study the momentum dependence of the gaps, Figs. 3(b1)–3(b4) display the band structure along four cuts (cuts 1–4) as labeled in Fig. 3(a). Both Δ_1 and Δ_2 vary significantly with momentum. The closer the band degeneracy points (points A, C, and E), the larger the Δ_1 . As shown in Fig. 2(d), the gap size of Δ_1 can reach ~ 600 meV. When approaching the 3D BZ boundary, the intersection between the main bands becomes deeper and deeper and mixes with the $4f$ -electron state of Eu, resulting in Δ_1 that is almost closed

or indistinguishable [30]. However, the CDW gap Δ_2 seems to present an opposite trend. Spectra along the main band formed “underlying FS” are shown in Fig. 3(c) together with spectra (dotted line) from a polycrystalline Au foil in electronic contact with the sample. The size of gap Δ_2 is extracted from the leading-edge midpoint position of EDCs, indicated by a black double-headed arrow. Δ_2 shows an evident momentum dependence. Figure 3(d) summarizes the gap size as a function of k_y , which shows that the gap value is the largest near the 3D BZ boundary and drastically decreases while approaching the band degeneracy points. At 30 K, the maximum and minimum gap sizes are ~ 180 and ~ 130 meV, respectively. At 240 K, the maximum gap value can reach ~ 230 meV, and the minimum gap value is ~ 170 meV. In FS nesting-driven CDW systems, gap variations along the underlying FS are consistently observed and commonly attributed to imperfect nesting [16,23]. In addition, the rapidly decreasing behavior of the CDW gap in the vicinity of band degeneracy points is reminiscent of the effect of band hybridization on CDW previously reported in the $R\text{Te}_3$ [35,36]. According to the model proposed by Grigoriev *et al.*, the band anticrossing near the Fermi level competes with CDW in the rare-earth telluride. The interplay between these two instabilities can reasonably explain the suppression of the CDW gap near the band degeneracy points [36]. Furthermore, another factor needs to be considered: the opening of Δ_1 would inevitably push parts of spectral weight upwards, thus narrowing the distance between the EDCs leading edge and E_F , especially around the band degeneracy points [30]. In addition, we also note an unusual temperature dependence of the CDW gap size below the E_F .

Finally, the temperature evolution of the CDW gap was studied. Figures 4(a1)–4(a8) show the detailed temperature

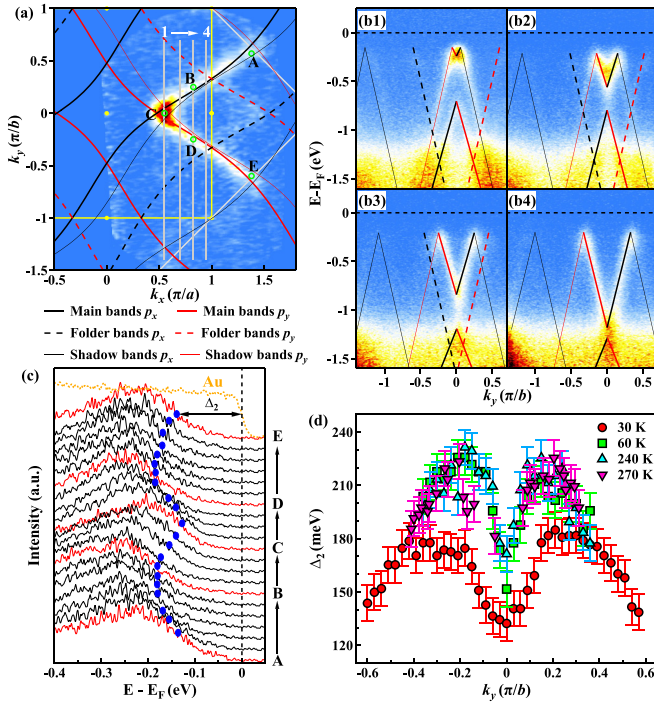


FIG. 3. (a) The constant energy map integrated over 20 meV, centered at binding energies $E_B = 0.2$ eV. (b1)–(b4) ARPES image plots along the k_y direction for $k_x = 0.55, 0.7, 0.82,$ and 0.95 (in π/a units) at $T = 60$ K. The lines represent band dispersion serving as a guide for the eyes (see legend). (c) EDCs at the main band from A to E at 30 K, along with reference Au spectra (dotted line). The points A, B, C, D, E are represented by empty circles as shown in (b). (d) Momentum-dependent energy gap Δ_2 at 30, 60, 240, and 270 K. The gap size is defined with respect to the leading edge of the spectra.

evolution of the ARPES images measured along a representative momentum cut [as shown in Fig. 3(a) white line 3] from 30 to 300 K. Δ_2 remains open at 300 K, which is consistent with the CDW phase transition that occurs well above room temperature in EuTe₄ [27,28]. A remarkable feature is that Δ_2 changes nonmonotonically with temperature. Figure 4(b) summarizes the extracted Δ_2 gap sizes at points B (green)

and D (blue). As temperature increases, the gap size keeps increasing until ~ 150 K and then gradually decreases. Such behavior deviates from the prediction of traditional CDW theory, which suggests the gap should follow a BCS curve [4]. It is worth noting that EuTe₄ is a semiconductor, and its chemical potential should be temperature dependent. The shift of chemical potential may strongly influence the sizes of Δ_2 . However, according to the change in the spectral weight of the Eu 4*f* electrons and the evolution of the Δ_1 center position, we speculate that the chemical potential plays almost no role in the anomalous increase in the magnitude of Δ_2 with increasing temperature and may only have a dominant role in the reduction of Δ_2 above 200 K [30]. A similar abnormal temperature-dependent CDW gap was observed in EuSbTe₃, and the higher binding energy gap's temperature evolution was considered to play a role [34]. However, this scenario does not apply here. First, the position of gap Δ_1 is far from the CDW gap at all temperatures at the momentum we measured, which could hardly affect the CDW gap Δ_2 . Second, the CDW gaps at measured temperatures have similar momentum dependence [Figs. 3(d) and 4(b)], which means that the temperature evolution of the CDW gap at the underlying FS should be the same, regardless of the size of the Δ_1 . It further proves that the anomalous temperature dependence of CDW gap Δ_2 is independent of the high energy gap Δ_1 . Furthermore, as mentioned above, a relative difference exists in the phase and mechanism of CDW distortion between the Te square bilayer and the monolayer [28,29]. However, this effect is not distinguished from the evolution of electronic structure. But, as previously reported in EuTe₄, the interaction between the bilayer and the monolayer CDWs may lead to hysteresis and a relatively large CDW gap in the heating branch [28]. However, it is worth noting that the CDW gap has begun to increase with the temperature increase before the onset of hysteresis. Therefore, other reasons may lead to the sharp decrease of the CDW gap at low temperatures, such as the emergence of a hidden order that suppresses the CDW. More experimental and theoretical works are required to explore such an abnormal behavior of the temperature-dependent CDW gap.

To conclude, based on the systematic ARPES measurement, a detailed analysis of the observed electronic structure

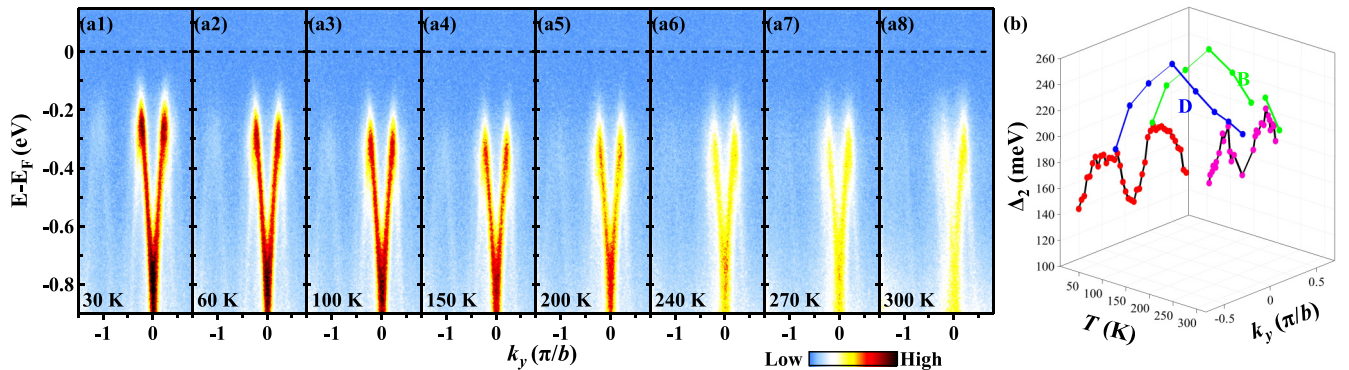


FIG. 4. (a1)–(a8) ARPES data of EuTe₄ along the same direction as in Fig. 3(b3) at the labeled temperatures. (b) Summary of the CDW gap Δ_2 . Green and blue dots represent the temperature-dependent CDW gap at points B and D, as indicated in Fig. 3(a), respectively. The red and magenta dots show the momentum-dependent CDW gap at 30 and 270 K, respectively.

on EuTe_4 single crystals was presented, suggesting that the FS nesting along b^* drives the CDW modulation results in its FS reconstruction and leaves a relatively large CDW gap that opens over the whole FS. The CDW modulation vector $q \approx 0.67b^*$ is exact from a twofold symmetric low-lying electronic structure. At higher binding energy, the interaction between the different orbits of the main bands introduces an extra band gap, Δ_1 , which should be one of the main reasons for the anisotropic CDW gap. Moreover, the temperature-dependent data reveal that the CDW gap exhibits abnormal behavior simultaneously with increasing temperature. Our

findings provide detailed information and critical insight into understanding FS nesting-driven CDW states on the electronic structure.

This work was supported by the National Natural Science Foundation of China (Grants No. 12074436 and No. 11874264), the Science and Technology Innovation Program of Hunan province (Grant No. 2022RC3068), the Innovation-driven Plan in Central South University (Grant No. 2016CXS032), and the Natural Science Foundation of Shanghai (Grant No. 17ZR1443300).

- [1] E. Dagotto, *Science* **309**, 257 (2005).
- [2] F. Flicker and J. van Wezel, *Nat. Commun.* **6**, 7034 (2015).
- [3] G. Grüner, *Rev. Mod. Phys.* **60**, 1129 (1988).
- [4] G. Grüner, *Density Waves in Solids* (Addison-Wesley, Reading, MA, 1994).
- [5] A. Damascelli, Z. Hussain, and Z.-X. Shen, *Rev. Mod. Phys.* **75**, 473 (2003).
- [6] S. Kirchner, S. Paschen, Q. Y. Chen, S. Wirth, D. L. Feng, J. D. Thompson, and Q. M. Si, *Rev. Mod. Phys.* **92**, 011002 (2020).
- [7] E. Morosan, H. W. Zandbergen, B. S. Dennis, J. Bos, Y. Onose, T. Klimczuk, A. P. Ramirez, N. P. Ong, and R. J. Cava, *Nat. Phys.* **2**, 544 (2006).
- [8] G. Ghiringhelli, M. Le Tacon, M. Minola, S. Blanco-Canosa, C. Mazzoli, N. B. Brookes, G. M. De Luca, A. Frano, D. G. Hawthorn, F. He *et al.*, *Science* **337**, 821 (2012).
- [9] E. H. Da Silva Neto, P. Aynajian, A. Frano, R. Comin, E. Schierle, E. Weschke, A. Gyenis, J. S. Wen, J. Schneeloch, Z. J. Xu *et al.*, *Science* **343**, 393 (2014).
- [10] R. Arpaia, S. Caprara, R. Fumagalli, G. De Vecchi, Y. Peng, E. Andersson, D. Betto, G. De Luca, N. Brookes, F. Lombardi *et al.*, *Science* **365**, 906 (2019).
- [11] Y. Y. Peng, R. Fumagalli, Y. Ding, M. Minola, S. Caprara, D. Betto, M. Bluschke, G. M. De Luca, K. Kummer, E. Lefrançois *et al.*, *Nat. Mater.* **17**, 697 (2018).
- [12] X. Zhu, J. Guo, J. Zhang, and E. Plummer, *Adv. Phys.: X* **2**, 622 (2017).
- [13] J. Schäfer, M. Sing, R. Claessen, E. Rotenberg, X. J. Zhou, R. E. Thorne, and S. D. Kevan, *Phys. Rev. Lett.* **91**, 066401 (2003).
- [14] G.-H. Gweon, J. D. Denlinger, J. A. Clack, J. W. Allen, C. G. Olson, E. D. DiMasi, M. C. Aronson, B. Foran, and S. Lee, *Phys. Rev. Lett.* **81**, 886 (1998).
- [15] V. Brouet, W. L. Yang, X. J. Zhou, Z. Hussain, N. Ru, K. Y. Shin, I. R. Fisher, and Z. X. Shen, *Phys. Rev. Lett.* **93**, 126405 (2004).
- [16] V. Brouet, W. L. Yang, X. J. Zhou, Z. Hussain, R. G. Moore, R. He, D. H. Lu, Z. X. Shen, J. Laverock, S. B. Dugdale, N. Ru, and I. R. Fisher, *Phys. Rev. B* **77**, 235104 (2008).
- [17] J. Li, Z. W. Chen, X. Y. Zhang, Y. X. Sun, J. Yang, and Y. Z. Pei, *NPG Asia Mater.* **9**, e353 (2017).
- [18] M. N. Ali, J. Xiong, S. Flynn, J. Tao, Q. D. Gibson, L. M. Schoop, T. Liang, N. Haldolaarachchige, M. Hirschberger, N. P. Ong, and R. J. Cava, *Nature (London)* **514**, 205 (2014).
- [19] M. S. Bahramy, O. J. Clark, B. J. Yang, J. Feng, L. Bawden, J. M. Riley, I. Markovi, F. Mazzola, V. Sunko, D. Biswas *et al.*, *Nat. Mater.* **17**, 21 (2018).
- [20] S.-Y. Liu, S.-X. Zhu, Q.-Y. Wu, C. Zhang, P. Bo Song, Y.-G. Shi, H. Liu, Z.-T. Liu, J.-J. Song, F.-Y. Wu *et al.*, *Res. Phys.* **30**, 104816 (2021).
- [21] P. Chen, W. W. Pai, Y. H. Chan, A. Takayama, C. Z. Xu, A. Karn, S. Hasegawa, M. Y. Chou, S. K. Mo, A. V. Fedorov, and T. C. Chiang, *Nat. Commun.* **8**, 516 (2017).
- [22] D. A. Zocco, J. J. Hamlin, K. Grube, J.-H. Chu, H.-H. Kuo, I. R. Fisher, and M. B. Maple, *Phys. Rev. B* **91**, 205114 (2015).
- [23] R. Lou, Y. P. Cai, Z. H. Liu, T. Qian, L. X. Zhao, Y. Li, K. Liu, Z. Q. Han, D. D. Zhang, J. B. He *et al.*, *Phys. Rev. B* **93**, 115133 (2016).
- [24] A. Kogar, A. Zong, P. E. Dolgirev, X. Z. Shen, J. Straquadine, Y. Q. Bie, X. R. Wang, T. Rohwer, I-Cheng Tung, Y. F. Yang *et al.*, *Nat. Phys.* **16**, 159 (2020).
- [25] Z. T. Liu, C. Zhang, Q. Y. Wu, H. Liu, B. Chen, Z. B. Yin, S. T. Cui, Z. Sun, S. X. Zhu, J. J. Song *et al.*, [arXiv:2203.03793](https://arxiv.org/abs/2203.03793).
- [26] S. Tadaki, N. Hino, T. Sambongi, K. Nomura, and F. Lévy, *Synth. Met.* **38**, 227 (1990).
- [27] D. Wu, Q. M. Liu, S. L. Chen, G. Y. Zhong, J. Su, L. Y. Shi, L. Tong, G. Xu, P. Gao, and N. L. Wang, *Phys. Rev. Mater.* **3**, 024002 (2019).
- [28] B. Q. Lv, A. Zong, D. Wu, A. V. Rozhkov, B. V. Fine, S. D. Chen, M. Hashimoto, D. H. Lu, M. Li, Y. B. Huang *et al.*, *Phys. Rev. Lett.* **128**, 036401 (2022).
- [29] A. Pathak, M. K. Gupta, R. Mittal, and D. Bansal, *Phys. Rev. B* **105**, 035120 (2022).
- [30] See Supplemental Material at <http://link.aps.org/supplemental/10.1103/PhysRevB.106.L201108> for additional data of EuTe_4 .
- [31] X. F. Tang, Y. X. Duan, F. Y. Wu, S. Y. Liu, C. Zhang, Y. Z. Zhao, J. J. Song, Y. Luo, Q. Y. Wu, J. He *et al.*, *Phys. Rev. B* **99**, 125112 (2019).
- [32] S. X. Zhu, C. Zhang, Q. Y. Wu, X. F. Tang, H. Liu, Z. T. Liu, Y. Luo, J. J. Song, F. Y. Wu, Y. Z. Zhao *et al.*, *Phys. Rev. B* **103**, 115108 (2021).
- [33] H. Yao, J. A. Robertson, E.-A. Kim, and S. A. Kivelson, *Phys. Rev. B* **74**, 245126 (2006).
- [34] C.-C. Fan, J.-S. Liu, K.-L. Zhang, W.-L. Liu, X.-L. Lu, Z.-T. Liu, D. Wu, Z.-H. Liu, D.-W. Shen, and L.-X. You, *Chin. Phys. Lett.* **35**, 077104 (2018).
- [35] H.-M. Eiter, M. Lavagnini, R. Hackl, E. A. Nowadnick, A. F. Kemper, T. P. Devereaux, J.-H. Chu, J. G. Analytis, I. R. Fisher, and L. Degiorgi, *Proc. Natl. Acad. Sci. USA* **110**, 64 (2013).
- [36] P. D. Grigoriev, A. A. Sinchenko, P. A. Vorobyev, A. Hadj-Azzem, P. Lejay, A. Bosak, and P. Monceau, *Phys. Rev. B* **100**, 081109(R) (2019).